



# Isothermal pressure-derived metastable states in 2D hybrid perovskites showing enduring bandgap narrowing

HPSTAR  
577-2018

Gang Liu<sup>a,1,2</sup>, Jue Gong<sup>b,1</sup>, Lingping Kong<sup>a,2</sup>, Richard D. Schaller<sup>c,d</sup>, Qingyang Hu<sup>a</sup>, Zhenxian Liu<sup>e</sup>, Shuai Yan<sup>f</sup>, Wenge Yang<sup>a</sup>, Constantinos C. Stoumpos<sup>c</sup>, Mercouri G. Kanatzidis<sup>c</sup>, Ho-kwang Mao<sup>a,g,2</sup>, and Tao Xu<sup>b,2</sup>

<sup>a</sup>Center for High Pressure Science and Technology Advanced Research, 201203 Shanghai, China; <sup>b</sup>Department of Chemistry and Biochemistry, Northern Illinois University, DeKalb, IL 60115; <sup>c</sup>Department of Chemistry, Northwestern University, Evanston, IL 60208; <sup>d</sup>Center for Nanoscale Materials, Argonne National Laboratory, Argonne, IL 60439; <sup>e</sup>Institute of Materials Science, Department of Civil and Environmental Engineering, The George Washington University, Washington, DC 20052; <sup>f</sup>Shanghai Institute of Applied Physics, Chinese Academy of Sciences, 201204 Shanghai, China; and <sup>g</sup>Geophysical Laboratory, Carnegie Institution of Washington, Washington, DC 20015

Contributed by Ho-kwang Mao, June 23, 2018 (sent for review May 30, 2018; reviewed by Peter Lazor and Zhiqun Lin)

**Materials in metastable states, such as amorphous ice and supercooled condensed matter, often exhibit exotic phenomena. To date, achieving metastability is usually accomplished by rapid quenching through a thermodynamic path function, namely, heating–cooling cycles. However, heat can be detrimental to organic-containing materials because it can induce degradation. Alternatively, the application of pressure can be used to achieve metastable states that are inaccessible via heating–cooling cycles. Here we report metastable states of 2D organic–inorganic hybrid perovskites reached through structural amorphization under compression followed by recrystallization via decompression. Remarkably, such pressure-derived metastable states in 2D hybrid perovskites exhibit enduring bandgap narrowing by as much as 8.2% with stability under ambient conditions. The achieved metastable states in 2D hybrid perovskites via compression–decompression cycles offer an alternative pathway toward manipulating the properties of these “soft” materials.**

metastable states | perovskite | pressure | compression–decompression | bandgap

**M**etastable materials can, in some cases, exhibit striking properties that are absent in thermodynamically stable states, and are of great significance in applications such as supramolecular polymers, graphene adlayers, and high-entropy alloys (1–4). The most frequently adopted method to achieve metastable states (e.g., supercooled transient liquid) is through fast quenching from a high temperature (5, 6). Such a heating/quenching strategy has limited utility for materials that are vulnerable to high temperature, such as organic-containing materials. Considering the fact that heat is a path function in connecting two thermodynamic states of a material, in which the detailed path depends on the structural and energetic landscape of the system, it follows that not all material phases are accessible via heating–cooling cycles. This is best exemplified by the impossible graphite-to-diamond conversion under ambient pressure, regardless of temperature. Moreover, the traditional fast-cooling path only allows materials to inherit properties from high-temperature states. This is not necessarily a path that can stretch to other thermodynamic regions with new properties. As such, it is imperative to explore other thermodynamic routes rather than temperature to access novel metastable states with ambient stability, while protecting the materials from thermal-induced damage.

Here, we use pressure, i.e., compression–decompression cycles, as an alternative thermodynamic method to drive materials to their metastable states that are not available via heating pathways. Analogous to a heating–cooling cycle that first elevates the entropy (disordering) of materials (6, 7), followed by deliberately reducing the entropy (ordering) to force the materials to be trapped in a metastable state, compression–decompression cycles can also control such an order → disorder → reordering process (8–12).

Halide perovskite solar cells have attracted ever-growing scientific interest due to their superior photovoltaic properties and simple device manufacturing processes (13–16). Moreover, 2D metal halide perovskites have become highly promising semiconductors because of their high degree of structural flexibility and tunable optoelectronic properties (17–19). They have a general formula of  $(A')_2(A)_{n-1}M_nX_{3n+1}$ , where  $A = Cs^+$ ,  $CH_3NH_3^+$  (MA),  $HC(NH_2)_2^+$  (FA),  $M = Ge^{2+}$ ,  $Sn^{2+}$ ,  $Pb^{2+}$  and  $X = Cl^-$ ,  $Br^-$ ,  $I^-$ , are the perovskite components, and  $A'^+$  =  $RNH_3$  is an organic spacer, such as  $CH_3(CH_2)_3NH_3^+$  (BA). These heat-vulnerable organic–inorganic hybrid materials behave as natural multiple quantum wells, with the semiconducting perovskite layers representing the wells and the insulating organic spacers representing the barriers. The width of the barrier is fixed and depends only on the length of the  $A'$  cation, while the width of the well can be adjusted by varying the thickness of perovskite slabs, which is defined by the  $n$  variable in  $(A')_2(A)_{n-1}M_nX_{3n+1}$ . Here, we demonstrate that hydrostatic pressure represents a precise tool to drive 2D hybrid perovskites to their metastable states with important changes in materials properties. We employed a combination of in situ high-pressure experiments at room temperature (i.e., isothermal) to comprehensively characterize a series of 2D  $(C_4H_9NH_3)_2(CH_3NH_3)_{n-1}Pb_nI_{3n+1}$  [ $(BA)_2(MA)_{n-1}Pb_nI_{3n+1}$ ].

## Significance

**Metastable materials often exhibit unexpected striking properties that are not available in stable state. While metastable states are generally achieved by rapid cooling of materials from high temperature, it is imperative to explore other nonthermal routes to access metastable states, especially for heat-vulnerable materials. Here, we report that work by pressure, namely, a compression–decompression cycle under ambient temperature, can drive thermosusceptible organic–inorganic hybrid perovskites to their metastable state, in which the perovskites show enduring bandgap narrowing by significantly broadened solar absorption. This pressure-derived route provides a fundamental path to obtain metastable materials with unprecedented performance.**

Author contributions: G.L., L.K., H.-k.M., and T.X. designed research; G.L., L.K., R.D.S., and M.G.K. performed research; J.G., R.D.S., Q.H., Z.L., S.Y., W.Y., C.C.S., and M.G.K. contributed new reagents/analytic tools; G.L., L.K., and Q.H. analyzed data; and G.L., J.G., R.D.S., M.G.K., and T.X. wrote the paper.

Reviewers: P.L., Uppsala University; and Z.L., Georgia Institute of Technology.

The authors declare no conflict of interest.

Published under the PNAS license.

<sup>1</sup>G.L. and J.G. contributed equally to this work.

<sup>2</sup>To whom correspondence may be addressed. Email: liugang@hpstar.ac.cn, konglp@hpstar.ac.cn, hmao@ciw.edu, or txu@niu.edu.

This article contains supporting information online at [www.pnas.org/lookup/suppl/doi:10.1073/pnas.1809167115/-DCSupplemental](http://www.pnas.org/lookup/suppl/doi:10.1073/pnas.1809167115/-DCSupplemental).

Published online July 23, 2018.

$n = 1, 2, 3, 4$ ] perovskites. These are model photovoltaic material systems with layered structures that promise superior tolerance to moisture (18). By using pressure-driven order  $\rightarrow$  disorder  $\rightarrow$  re-order cycles, we observed a significant bandgap narrowing in 2D perovskites, especially in  $(\text{BA})_2(\text{MA})_2\text{Pb}_3\text{I}_{10}$  ( $n = 3$ ), which persists after decompression. We show that a metastable state created from structural reconstruction is the origin of bandgap narrowing in pressure-treated perovskites.

## Results and Discussion

To explore the pressure-driven order  $\rightarrow$  disorder  $\rightarrow$  reorder evolution and the related materials properties, we first performed in situ high-pressure optical absorption spectroscopy and structural characterizations on polycrystalline samples of the 2D perovskites  $(\text{BA})_2\text{PbI}_4$  ( $n = 1$ ),  $(\text{BA})_2(\text{MA})_2\text{Pb}_3\text{I}_{10}$  ( $n = 3$ ), and  $(\text{BA})_2(\text{MA})_3\text{Pb}_4\text{I}_{13}$  ( $n = 4$ ). The ambient crystal structures and bandgaps of these 2D perovskites are shown in *SI Appendix, Figs. S1–S4*. The bandgap magnitudes agree well with the previously reported values and are consistent with quantum confinement effects (17, 20). As shown in Fig. 1*A–C*, all three 2D perovskites show strong pressure-dependent bandgap evolution and various inflections between blueshift and redshift. For  $(\text{BA})_2\text{PbI}_4$  ( $n = 1$ ), the absorption edge redshifts from 542 nm at ambient pressure to 708 nm at 8.3 GPa, and then blueshifts to 680 nm as pressure further increases to 17.8 GPa (Fig. 1*A*). Comparatively,  $(\text{BA})_2(\text{MA})_2\text{Pb}_3\text{I}_{10}$  ( $n = 3$ ) shows an absorption edge that increases in wavelength from 638 nm at ambient pressure to a maximum of 698 nm at 2.5 GPa, and then declines to 610 nm at 10.1 GPa, followed by a rise as pressure further increases (Fig. 1*B*). For higher- $n$  2D perovskite, e.g.,  $(\text{BA})_2(\text{MA})_3\text{Pb}_4\text{I}_{13}$  ( $n = 4$ ), two regimes of bandgap redshift are observed (Fig. 1*C*). The absorption edge first reaches a peak value of 719 nm at  $\sim 1.5$  GPa, and then quickly blueshifts to 627 nm at 4.7 GPa, followed by another redshift to 780 nm at 20.8 GPa.

The pressure dependences of bandgaps of 2D perovskites are also shown in the corresponding Tauc plots (*SI Appendix, Figs. S5–S9*). As shown in Fig. 1*D*, at a mild pressure range of less than 10 GPa, all 2D perovskites undergo a general bandgap narrowing until the respective pressure inflections, which can be understood by the easier layer-to-layer compression that results in more overlapped electron density function wave coupling between the Pb *s* and I *p* orbitals (12, 21). We also note a delicate trend of bandgap evolution in  $(\text{BA})_2\text{PbI}_4$  ( $n = 1$ ) before the monotonic bandgap narrowing, where a slight increase from 2.29 eV to

2.38 eV occurs at low pressures of 1 atm to 0.55 GPa. Such distinctive behavior is attributable to the unique single inorganic sheet characteristic that directly forms a structural distortion without homogeneous and long-range order along all three dimensions. Therefore, decreases in Pb–I–Pb bond angles and bond lengths occur simultaneously in the initial and mild compressions, where the former lead to an enlarged bandgap while the latter act to counteract this trend by causing bandgap narrowing (Scheme 1).

Interestingly, by connecting the inflection point (solid red line in Fig. 1*D*) between the bandgap redshift and blueshift of all perovskites, we can see the decreasing trend of inflection pressures with increased layer thickness  $n$  in the perovskites. This observation is consistent with the systematically varying volumetric proportion of the inorganic layer in each compound as a function of  $n$ , as described by  $2L/D$  ( $L$  and  $D$  denote the thickness of inorganic layer and longitudinal length of the perovskite unit cell, respectively, as shown in *SI Appendix, Fig. S10*). Considering that space between inorganic layers is filled with the highly compressible organic  $\text{BA}^+$  groups, and the observation that bandgap broadening is associated with atomic distortion in the inorganic layers, our discovery indicates that the  $\text{BA}^+$  content plays a pivotal role in controlling the degree of structural distortion in the inorganic layers, thereby affecting the bandgap evolution. To explore the root cause of bandgap evolution and derive structure–property relationships, we performed in situ synchrotron pressure-dependent structural characterization. These experiments were crucial in helping us select the optimal route to achieve wide materials tuning even after the applied pressure is totally released.

Fig. 2*A–C* shows typical X-ray diffraction (XRD) patterns of  $(\text{BA})_2\text{PbI}_4$  ( $n = 1$ ),  $(\text{BA})_2(\text{MA})_2\text{Pb}_3\text{I}_{10}$  ( $n = 3$ ), and  $(\text{BA})_2(\text{MA})_3\text{Pb}_4\text{I}_{13}$  ( $n = 4$ ), respectively. As pressure increases, the diffraction peaks of all 2D perovskites broaden, which is attributed to structural distortion and increasing amorphization (6, 8). For  $(\text{BA})_2\text{PbI}_4$  ( $n = 1$ ), high atomic distortion and amorphization take place at 8.0 GPa, as indicated by the much broader peak centered around  $12^\circ$  (Fig. 2*A*). Likewise, the pressure-induced atomic distortion and amorphization are also observed in 2D perovskite members with higher  $n$  values, and thus can be regarded as a general compression mechanism. However, the pressure regions that cause atomic distortion start to decrease with greater  $n$  values. For  $(\text{BA})_2(\text{MA})_2\text{Pb}_3\text{I}_{10}$  ( $n = 3$ ) and  $(\text{BA})_2(\text{MA})_3\text{Pb}_4\text{I}_{13}$  ( $n = 4$ ), the order–disorder structural distortions appear around 4.5 and 2.4 GPa, respectively. The  $d$  spacings were obtained by fitting the complete high-pressure

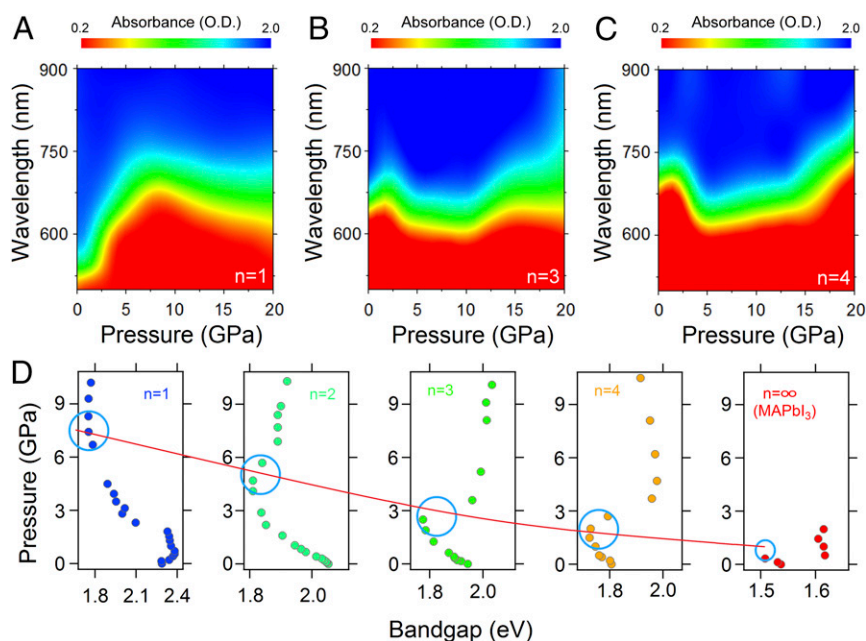
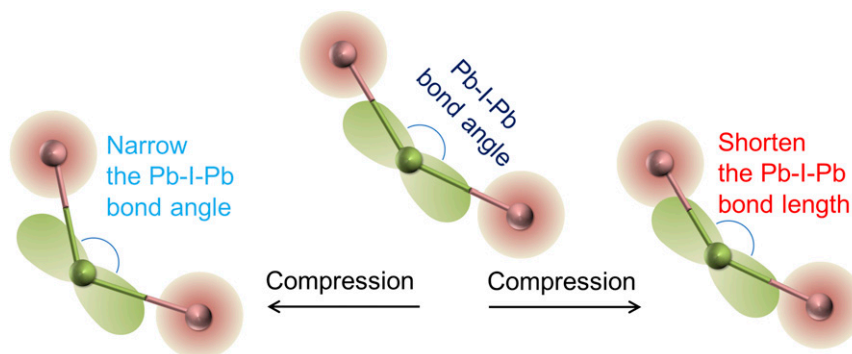


**Fig. 1.** Absorbance of 2D perovskites under pressure conditions. (*A–C*) Contour plots of pressure-dependent absorbance of (*A*)  $(\text{BA})_2\text{PbI}_4$  ( $n = 1$ ), (*B*)  $(\text{BA})_2(\text{MA})_2\text{Pb}_3\text{I}_{10}$  ( $n = 3$ ), and (*C*)  $(\text{BA})_2(\text{MA})_3\text{Pb}_4\text{I}_{13}$  ( $n = 4$ ). (*D*) Pressure-dependent bandgap evolutions of  $(\text{BA})_2\text{PbI}_4$  ( $n = 1$ ) (blue),  $(\text{BA})_2\text{MAPb}_2\text{I}_7$  ( $n = 2$ ) (light green),  $(\text{BA})_2(\text{MA})_2\text{Pb}_3\text{I}_{10}$  ( $n = 3$ ) (green),  $(\text{BA})_2(\text{MA})_3\text{Pb}_4\text{I}_{13}$  ( $n = 4$ ) (orange) and  $\text{MAPbI}_3$  ( $n = \infty$ ) (red). Data of  $(\text{BA})_2\text{MAPb}_2\text{I}_7$  and  $\text{MAPbI}_3$  are from refs. 12 and 10, respectively. Red line represents a guide to eye that passes through the bandgap inflection pressure points (indicated by light blue circles), and shows a decreasing trend as  $n$  increases.



**Scheme 1.** Schematic illustration of Pb–I–Pb bonds in  $(\text{BA})_2\text{PbI}_4$  under compression. Under initial compression from 1 atm to 0.5 GPa, the slight blueshifts of bandgap can be understood from the reduced orbital overlaps between Pb and I caused by decreased Pb–I–Pb bond angles. As pressure continues to increase, perovskite lattice is compressed, with the bond lengths of Pb–I–Pb being unavoidably shortened, leading to the increased electronic wave function overlap between Pb and I, and thereby accounting for the narrowed optical bandgap.

XRD patterns (*SI Appendix, Figs. S11–S13*). As shown in Fig. 2D and *SI Appendix, Figs. S11–S13*, clear anisotropic compression behaviors are present in all investigated 2D perovskites ( $n = 1, 2, 3$ , and 4). A comprehensive mechanism can be summarized as two-step compressions dominated by layer-to-layer compression at low pressures and intralayer compression at relatively high pressures. These are attributed to the softer organic and less compressible inorganic sublattices, respectively. Here, the layer-to-layer compression denotes the compression perpendicular to the inorganic sheet, while the intralayer compression describes the compressions in the plane of the inorganic sheet (*SI Appendix, Fig. S1*).

The structural evolutions can be correlated with changes in the optical bandgaps during compression. As summarized in Fig. 2E, for all 2D perovskites, the pressures corresponding to bandgap inflections agree well with the respective atomic distortion regions. This confirms that the origin of the bandgap blueshift is structural distortion which modulates the overlap between the Pb *s* and I *p* orbitals. Furthermore, a roughly linear relationship between characteristic pressure and  $1/n$  is observed, giving a more comprehensive picture of structure–property relationship.

Since ambient properties are the most relevant for applications, we monitored the lattice and optical response of 2D perovskites under stepwise decompression from the high-pressure amorphous state to 1 atm at room temperature. For  $(\text{BA})_2(\text{MA})_2\text{Pb}_3\text{I}_{10}$  ( $n =$

3), by extrapolating the linear portion of the  $(\alpha d h \nu)^2$  versus energy  $h\nu$  plot, direct bandgaps of 1.78 and 1.94 eV were estimated after decompression from 26 GPa and before compression, respectively (Fig. 3A). This 8.2% bandgap narrowing is the largest pressure-driven change among all reported photovoltaic perovskites to date. The narrow bandgap signifies a significant improvement in light absorption (22). We also note that, after stepwise decompression, the bandgap of  $(\text{BA})_2(\text{MA})_2\text{Pb}_3\text{I}_{10}$  ( $n = 3$ ) is even narrower than that of as-prepared higher- $n$  2D perovskite member  $(\text{BA})_2(\text{MA})_3\text{Pb}_4\text{I}_{13}$  ( $n = 4$ ) (1.81 eV, *SI Appendix, Figs. S4 and S14*). Our General Structure System Analysis (GSAS) refinement of the XRD pattern (Fig. 3B) found that the decompressed  $(\text{BA})_2(\text{MA})_2\text{Pb}_3\text{I}_{10}$  ( $n = 3$ ) recrystallized to the expected 2D layered perovskite structure with an orthorhombic *C2ab* symmetry like the as-prepared sample but with widened Pb–I–Pb bond angles (*SI Appendix, Table S1*), which corroborates the narrowed bandgap.

We then calculated the total energy for both the pressure-treated structure and as-prepared (ground state) structure under the density functional theory (DFT) framework. As shown in Fig. 3C, the pressure-treated structure has higher enthalpy at ambient condition than that of the as-prepared sample ( $\Delta H = 0.114$  eV/unit cell); thus the as-prepared sample can be demonstrated as ground state with thermodynamic stable characteristic, while the pressure-treated one is metastable. However, we emphasized here that there

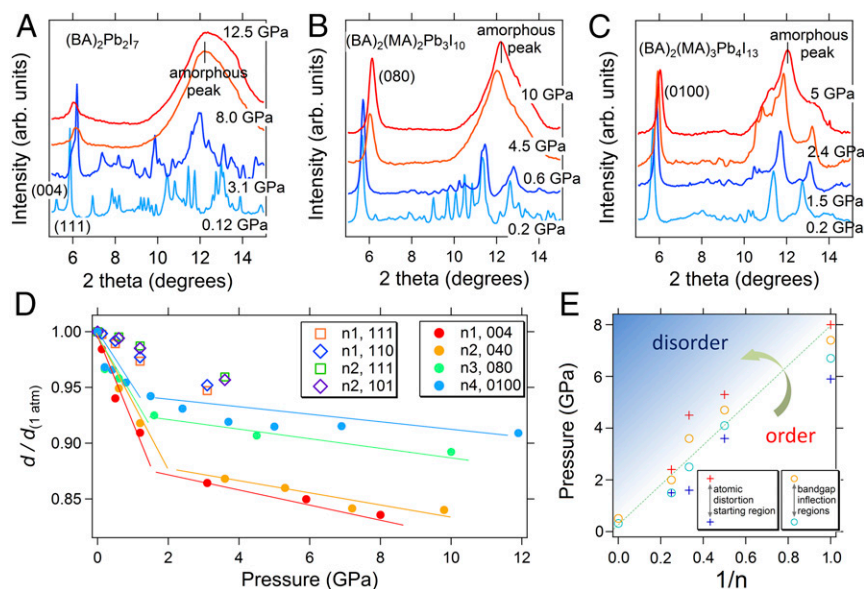


**Fig. 2.** Structural evolutions of 2D perovskites under compression. (A–C) Pressure-dependent XRD patterns of (A)  $(\text{BA})_2\text{PbI}_4$ , (B)  $(\text{BA})_2(\text{MA})_2\text{Pb}_3\text{I}_{10}$ , and (C)  $(\text{BA})_2(\text{MA})_3\text{Pb}_4\text{I}_{13}$ . (D) Compressibilities (lattice shrinkages) of 2D perovskites by means of  $d/d_{(1 \text{ atm})}$  [red,  $(\text{BA})_2\text{PbI}_4$  ( $n = 1$ ); yellow,  $(\text{BA})_2\text{MAPb}_2\text{I}_7$  ( $n = 2$ ); green,  $(\text{BA})_2(\text{MA})_2\text{Pb}_3\text{I}_{10}$  ( $n = 3$ ); blue,  $(\text{BA})_2(\text{MA})_3\text{Pb}_4\text{I}_{13}$  ( $n = 4$ )]. Lines represent linear fittings of layer-to-layer lattice shrinkage points in both low- and high-pressure ranges, thus showing the trends of lattice parameter evolutions at different rates. (E) Summary of structural amorphization pressure points, as inferred from XRD patterns (crosses) and from bandgap inflections (circles), on  $(\text{BA})_2\text{PbI}_4$  ( $n = 1$ ),  $(\text{BA})_2\text{MAPb}_2\text{I}_7$  ( $n = 2$ ),  $(\text{BA})_2(\text{MA})_2\text{Pb}_3\text{I}_{10}$  ( $n = 3$ ),  $(\text{BA})_2(\text{MA})_3\text{Pb}_4\text{I}_{13}$  ( $n = 4$ ), and  $\text{MAPbI}_3$  ( $n = \infty$ ). Dashed line represents a guide to eye that outlines the approximate regions of order and disorder lattice structures. Data of  $(\text{BA})_2\text{MAPb}_2\text{I}_7$  and  $\text{MAPbI}_3$  are from refs. 12 and 10, respectively.

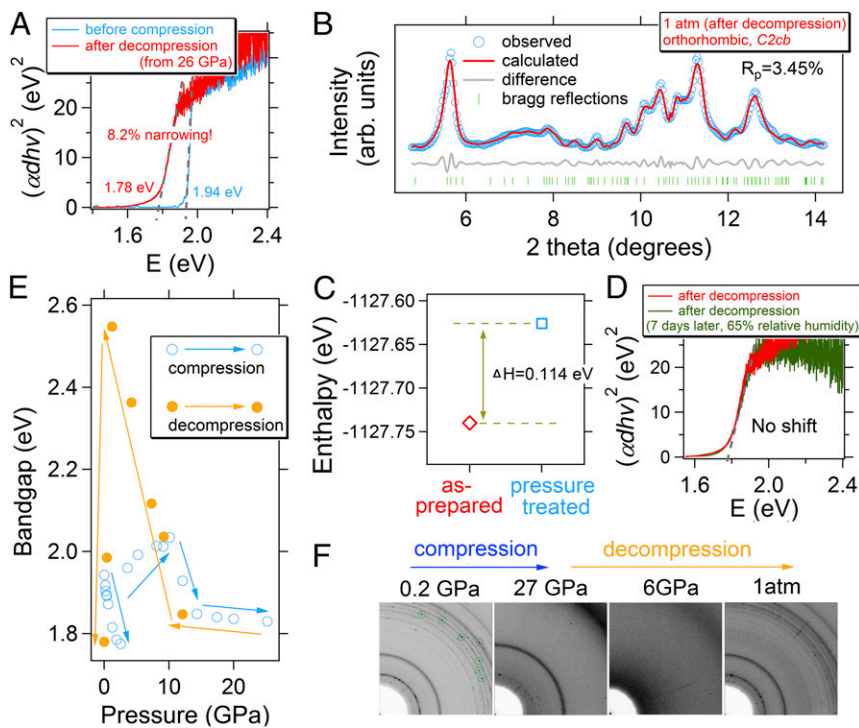


**Fig. 3.** Pressure-dependent bandgap and structural evolution of  $(\text{BA})_2(\text{MA})_2\text{Pb}_3\text{I}_{10}$  ( $n = 3$ ) under compression–decompression cycle. (A) Tauc plots before compression (blue) and after the decompression (red), with 8.2% ambient bandgap narrowing observed. (B) XRD pattern measured after decompression from 27 GPa. (C) Comparison of enthalpy per unit cell before compression (as-prepared) and after decompression (pressure-treated). (D) Tauc plot for the same decompressed  $(\text{BA})_2(\text{MA})_2\text{Pb}_3\text{I}_{10}$  ( $n = 3$ ) sample but exposed to wet air (65% relative humidity) for 1 wk. (E) Comparison of bandgaps measured during compression (hollow blue dots) and decompression (solid yellow dots) under various pressures. Yellow lines are guides to the eye showing the bandgap trends during decompression. (F) Diffraction pattern images measured during compression and decompression processes.

is no change for the narrowed bandgap in the pressure-treated sample even after exposure to 65% relative humidity air for 1 wk (Fig. 3D), from which we can conclude a long-term stable behavior presumably because of a sufficiently high activation barrier.

In addition, we discovered that, instead of following the original path of bandgap evolution during compression, the decompression of  $(\text{BA})_2(\text{MA})_2\text{Pb}_3\text{I}_{10}$  from 7.3 to 1.2 GPa undergoes an unusual bandgap widening from 2.12 eV to 2.55 eV (Fig. 3E and *SI Appendix*, Fig. S15). Such a bandgap evolution trend during decompression relates a different thermodynamic path, suggesting that the structure and properties exhibited by the pressure-treated samples are not memory effects from the high-pressure state (23, 24), but are associated with structural reconstruction during decompression. This claim can be further verified by scrutinizing the XRD patterns obtained during the compression and decompression processes. As shown in Fig. 3F, visible diffraction spots together with diffraction rings were observed at low-pressure 0.2 GPa during compression, indicating a dominant polycrystalline nature but with preferred orientation and unbalanced strain. At 6 GPa, under decompression, no sharp diffraction rings were observed, and X-ray amorphicity was apparent and even more obvious than at 27 GPa, where a broad diffraction ring was observed. Importantly, after full reduction to ambient pressure, clear diffraction rings without diffraction spots were observed, and most diffraction peaks broadened compared with before compression, thereby indicating an altered crystal microstructure with reduced grain size (25).

To further investigate the effects of pressure treatment, we discuss the light absorption properties of the other 2D perovskites after the compression–decompression process. Clearly, the pressure cycles presented above do not affect the bandgap of  $(\text{BA})_2\text{PbI}_4$  ( $n = 1$ ), which is direct at 2.28 eV after decompression from 28 GPa to ambient pressure (Fig. 4A and *SI Appendix*, Fig. S16). We further studied the bandgap magnitude when removing the applied pressure (*SI Appendix*, Fig. S17) and the ambient crystalline structure in decompressed  $(\text{BA})_2\text{PbI}_4$  ( $n = 1$ ) (*SI Appendix*, Fig. S18 and Table S2) and found a nearly unchanged route for bandgap evolution and a recovered structure after pressure treatment, affirming the largely unaffected thermodynamic state. Conversely,  $(\text{BA})_2(\text{MA})_3\text{Pb}_4\text{I}_{13}$  ( $n = 4$ ) exhibits a considerably narrowed bandgap of 1.74 eV after

decompression from 26 GPa to 1 atm, in contrast to the original 1.81 eV before compression (Fig. 4B). The modestly changed ambient state of  $(\text{BA})_2(\text{MA})_3\text{Pb}_4\text{I}_{13}$  ( $n = 4$ ) after pressure treatment can be further validated through the GSAS fitting of the XRD pattern (*SI Appendix*, Fig. S19 and Table S3). For

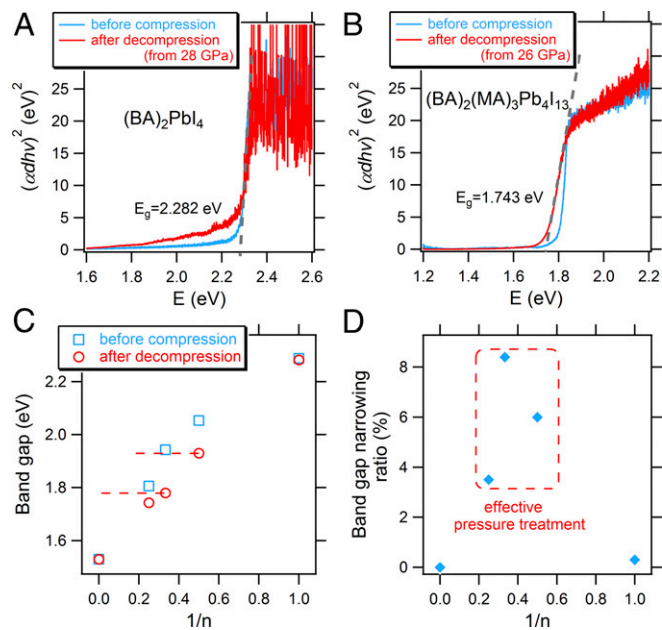


**Fig. 4.** Light absorption properties of 2D perovskites after compression–decompression cycles. (A and B) Tauc plots of (A)  $(\text{BA})_2\text{PbI}_4$  and (B)  $(\text{BA})_2(\text{MA})_3\text{Pb}_4\text{I}_{13}$ . Extrapolated bandgaps are shown for the samples measured after decompression. (C) Comparison of bandgaps on  $(\text{BA})_2\text{PbI}_4$  ( $1/n = 1$ ),  $(\text{BA})_2\text{MAPb}_2\text{I}_7$  ( $1/n = 0.5$ ),  $(\text{BA})_2(\text{MA})_2\text{Pb}_3\text{I}_{10}$  ( $1/n = 0.33$ ),  $(\text{BA})_2(\text{MA})_3\text{Pb}_4\text{I}_{13}$  ( $1/n = 0.25$ ), and  $\text{MAPbI}_3$  ( $1/n = 0$ ). (D) Bandgap narrowing ratio after pressure treatments for hybrid perovskites. Data of  $(\text{BA})_2\text{MAPb}_2\text{I}_7$  and  $\text{MAPbI}_3$  are from refs. 12 and 10, respectively.



solution), followed by rotary evaporation at 60 °C to obtain the product (26), while  $n\text{-C}_4\text{H}_9\text{NH}_2$  (BAI) solution was prepared by acidifying  $n\text{-C}_4\text{H}_9\text{NH}_2$  (BA, 99.5%) with excessive HI solution (13). The synthesis of  $(\text{BA})_2(\text{MA})_{n-1}\text{Pb}_n\text{I}_{3n+1}$  2D perovskites involves reactions of specific stoichiometric ratios of lead(II) oxide ( $\text{PbO}$ ,  $\geq 99.0\%$ ), HI, hypophosphorous acid ( $\text{H}_3\text{PO}_2$ , 50% wt/wt aqueous solution), and  $\text{CH}_3\text{NH}_3\text{Cl}$  in acid environments at boiling temperatures, followed by slow cooling to room temperature for precipitation, as detailed in ref. 17. In terms of  $\text{MAPbI}_3$ , it is synthesized by following methods reported in the literature (27). Specifically, equimolar of MAI and  $\text{PbI}_2$  were first dissolved in  $\gamma$ -Butyrolactone ( $\geq 99\%$ ) to form 1 M precursor solution. Next, the solution was heated at 110 °C on a hot plate for 3 h until black crystals of  $\sim 1.5$  mm size formed.

**In Situ Synchrotron High-Pressure Powder XRD.** In situ synchrotron high-pressure powder XRD experiments were carried out at beamline 15U of the Shanghai Synchrotron Radiation Facility (SSRF), Shanghai, China. Monochromatic X-ray with wavelength of 0.6199 Å was employed, and the incident X-ray beam was focused to a  $5 \mu\text{m} \times 5 \mu\text{m}$  spot. XRD patterns were collected with a MAR345 CCD detector. The samples were loaded in a symmetric-type diamond anvil cell (DAC) with a pair of 300  $\mu\text{m}$  culets and placed in a rhenium (Re) gasket hole with diameter of 120  $\mu\text{m}$ . It should be noted that methanol/ethanol cannot be used as pressure medium, since organic-inorganic hybrid samples are easily decomposed in polar solvent (28), and the gaseous pressure medium should also be employed prudently, since the low-pressure range could be easily jumped across during the gas loading process. Therefore, mineral oil was used as pressure-transmitting medium, which also can achieve a good hydrostatic pressure environment. Two ruby balls with diameters of 5  $\mu\text{m}$  were loaded in the sample chamber, and the pressure was determined by the ruby luminescence method (29). This method was also used in other high-pressure optical absorbance measurement as discussed in *In Situ High-Pressure Optical Absorption Spectroscopy*. The GSAS program was employed to refine the obtained experimental XRD profiles (30).

**In Situ High-Pressure Optical Absorption Spectroscopy.** In situ high-pressure optical absorption spectroscopy was performed at Infrared Lab of the National Synchrotron Light Source II (NSLS II) at Brookhaven National Laboratory and Center for Nanoscale Materials (CNM) at Argonne National Laboratory. The visible absorption measurements were performed between 10,000  $\text{cm}^{-1}$  and 25,000  $\text{cm}^{-1}$  and utilized a customized visible microscope system. Symmetric-type diamond anvil cell and a pair of Ila-type diamond

anvils with a culet size of 300  $\mu\text{m}$  were employed. Mineral oil was used as pressure-transmitting medium, and silicon oil was used to determine an absorbance baseline.

**Theoretical Calculations.** First-principles calculations were performed in the framework of DFT through the Vienna ab initio simulation package. (31) The exchange correlation functions are described by the Generalized Gradient Approximation under Perdew–Burke–Ernzerhof parametrization revised for solids (32). Projected augmented wave potentials model 14 valence electrons for Pb ( $5d^{10}6s^26p^2$ ), 7 for I ( $5s^25p^2$ ), 4 for C atoms ( $2s^22p^2$ ), 5 for N atoms ( $2s^22p^3$ ), and 1 for H ( $1s^1$ ). We used a plane-wave basis set with kinetic 550-eV energy cutoff that is sufficient to optimize the structure until forces acting on each atom are less than  $0.01 \text{ eV}\cdot\text{Å}^{-1}$ . We employed a Monkhorst mesh of  $4 \times 4 \times 1 k$  points for  $(\text{BA})_2\text{PbI}_4$  ( $n = 1$ ) phase and  $2 \times 1 \times 2 k$  points for  $(\text{BA})_2(\text{MA})_2\text{Pb}_3\text{I}_{10}$  ( $n = 3$ ). Crystal structures were directly taken from our XRD experiments. Selective dynamic relaxations were performed by tuning the values of lattice angles. For  $(\text{BA})_2\text{PbI}_4$  ( $n = 1$ ), only one Pb–I–Pb is available based on crystal symmetry. In  $(\text{BA})_2(\text{MA})_2\text{Pb}_3\text{I}_{10}$  ( $n = 3$ ), four Pb–I–Pb angles are allowed to change. Here we select two angles of Pb1–I4–Pb1 and Pb2–I3–Pb2 for building up a 2D energy profile. Atoms forming the related angles were not relaxed in geometrical optimization.

**ACKNOWLEDGMENTS.** We thank the staff from BL01B beamline of National Center for Protein Science Shanghai at Shanghai Synchrotron Radiation Facility for assistance during data collection. G.L., L.K., and H.-k.M. acknowledge support from the NSAF (U1530402). T.X. acknowledges the financial support from the US National Science Foundation (CBET-1150617 and DMR-1806152). High-pressure powder structure characterizations were performed at beamline 15U at SSRF. Optical measurements were made at the Infrared Laboratory at NSLS-II. The Infrared Laboratory is supported by the Consortium for Materials Properties Research in Earth Sciences under National Science Foundation Cooperative Agreement EAR 1606856 and the Department of Energy (DOE)/National Nuclear Security Administration under Grant DE-NA-0002006. NSLS-II is supported by the DOE Office of Science under Contract DE-SC0012704. Work at Northwestern University was supported by Grant SC0012541 from the US DOE, Office of Science (sample synthesis, processing, and structural characterization). Use of CNM, an Office of Science user facility, was supported by the US DOE, Office of Science, Office of Basic Energy Sciences, under Contract DE-AC02-06CH11357. The computational work was conducted on the SR10000-K1/52 supercomputing facilities of the Institute for Materials Research, Tohoku University.

- Sun W, et al. (2016) The thermodynamic scale of inorganic crystalline metastability. *Sci Adv* 2:e1600225.
- Korevaar PA, et al. (2012) Pathway complexity in supramolecular polymerization. *Nature* 481:492–496.
- Chen C, et al. (2018) Large local lattice expansion in graphene adlayers grown on copper. *Nat Mater* 17:450–455.
- Li Z, Pradeep KG, Deng Y, Raabe D, Tasan CC (2016) Metastable high-entropy dual-phase alloys overcome the strength-ductility trade-off. *Nature* 534:227–230.
- Handle PH, Loerting T, Sciortino F (2017) Supercooled and glassy water: Metastable liquid(s), amorphous solid(s), and a no-man's land. *Proc Natl Acad Sci USA* 114:13336–13344.
- Sharma SM, Sikka SK (1996) Pressure induced amorphization of materials. *Prog Mater Sci* 40:1–77.
- McQuarrie DA, Simon JD (1999) *Molecular Thermodynamics* (Univ Sci Books, Sausalito, CA).
- Hu QY, et al. (2015) Polymorphic phase transition mechanism of compressed coesite. *Nat Commun* 6:6630.
- Lü X, et al. (2016) Enhanced structural stability and photo responsiveness of  $\text{CH}_3\text{NH}_3\text{SnI}_3$  perovskite via pressure-induced amorphization and recrystallization. *Adv Mater* 28:8663–8668.
- Kong L, et al. (2016) Simultaneous band-gap narrowing and carrier-lifetime prolongation of organic-inorganic trihalide perovskites. *Proc Natl Acad Sci USA* 113:8910–8915.
- Liu G, et al. (2017) Pressure-induced bandgap optimization in lead-based perovskites with prolonged carrier lifetime and ambient retainability. *Adv Funct Mater* 27:1604208.
- Liu G, et al. (2017) Two regimes of bandgap red shift and partial ambient retention in pressure-treated two-dimensional perovskites. *ACS Energy Lett* 2:2518–2524.
- Kojima A, Teshima K, Shirai Y, Miyasaka T (2009) Organometal halide perovskites as visible-light sensitizers for photovoltaic cells. *J Am Chem Soc* 131:6050–6051.
- He M, et al. (2017) Meniscus-assisted solution printing of large-grained perovskite films for high-efficiency solar cells. *Nat Commun* 8:16045.
- Ye M, et al. (2017) Recent advances in interfacial engineering of perovskite solar cells. *J Phys D Appl Phys* 50:373002.
- He M, et al. (2016) Monodisperse dual-functional upconversion nanoparticles enabled near-infrared organolead halide perovskite solar cells. *Angew Chem Int Ed Engl* 55:4280–4284.
- Stoumpos CC, et al. (2016) Ruddlesden-Popper hybrid lead iodide perovskite 2D homologous semiconductors. *Chem Mater* 28:2852–2867.
- Tsai H, et al. (2016) High-efficiency two-dimensional Ruddlesden-Popper perovskite solar cells. *Nature* 536:312–316.
- Blanco JC, et al. (2017) Extremely efficient internal exciton dissociation through edge states in layered 2D perovskites. *Science* 355:1288–1292.
- Gao DH, Stoumpos CC, Farha OK, Hupp JT, Kanatzidis MG (2015) 2D homologous perovskites as light-absorbing materials for solar cell applications. *J Am Chem Soc* 137:7843–7850.
- Yin WJ, Yang JH, Kang J, Yan Y, Wei SH (2015) Halide perovskite materials for solar cells: A theoretical review. *J Mater Chem A* 3:8926–8942.
- Shockley W, Queisser HJ (1961) Detailed balance limit of efficiency of  $p$ - $n$  junction solar cells. *J Appl Phys* 32:510.
- Lin C, Smith JS, Sinogeikin SV, Shen G (2018) Experimental evidence of low-density liquid water upon rapid decompression. *Proc Natl Acad Sci USA* 115:2010–2015.
- Li Q, et al. (2017) High-pressure band-gap engineering in lead-free  $\text{Cs}_2\text{AgBiBr}_6$  double perovskite. *Angew Chem Int Ed Engl* 56:15969–15973.
- Birks LS, Friedman H (1946) Particle size determination from X-ray line broadening. *J Appl Phys* 17:687–692.
- Lee MM, Teuscher J, Miyasaka T, Murakami TN, Snaith HJ (2012) Efficient hybrid solar cells based on meso-structured organometal halide perovskites. *Science* 338:643–647.
- Saidaminov MI, et al. (2015) High-quality bulk hybrid perovskite single crystals within minutes by inverse temperature crystallization. *Nat Commun* 6:7586.
- Im JH, Jang IH, Pellet N, Grätzel M, Park NG (2014) Growth of  $\text{CH}_3\text{NH}_3\text{PbI}_3$  cuboids with controlled size for high-efficiency perovskite solar cells. *Nat Nanotechnol* 9:927–932.
- Mao HK, Xu J, Bell PM (1986) Calibration of the ruby pressure gauge to 800 kbar under quasi-hydrostatic conditions. *J Geophys Res* 91:4673–4676.
- Larson AC, von Dreele RB (1994) General Structure Analysis System (GSAS) (Los Alamos Natl Lab, Los Alamos, NM), Rep LAUR 86-748.
- Kresse G, Hafner J (1994) *Ab initio* molecular-dynamics simulation of the liquid-metal-amorphous-semiconductor transition in germanium. *Phys Rev B Condens Matter* 49:14251–14269.
- Perdew JP, et al. (2008) Restoring the density-gradient expansion for exchange in solids and surfaces. *Phys Rev Lett* 100:136406.